Journal of Alloys and Compounds 505 (2010) 428–433

Contents lists available at ScienceDirect

Journal of Alloys and Compounds

journal homepage: www.elsevier.com/locate/jallcom

Reductive synthesis of metal antimonides

Rebecca L. Kift, Timothy J. Prior*

Department of Chemistry, University of Hull, Cottingham Road, Hull, HU6 7RX, United Kingdom

ARTICLE INFO

Article history:
Received 25 March 2010
Received in revised form 3 June 2010
Accepted 13 June 2010
Available online 23 June 2010

Keywords:
Transition metal alloys and compounds
Gas–solid reactions
Phase diagram
Crystal structure
X-ray diffraction

ABSTRACT

A new low temperature synthetic route to binary and ternary metal antimonides is reported. Binary transition metal antimonides prepared include $CoSb_3$, $CoSb_2$, CoSb, NiSb, $NiSb_2$, Cu_2Sb and Mo_3Sb_7; new ternary compositions prepared include the series $Co_{1-x}Ni_xSb$ ($0.1 \leq x \leq 0.9$). The intermetallic SnSb has also been prepared by this route. The synthetic method is simple and does not require the use of very high temperatures, multi-step reactions or reaction under vacuum. Compounds were synthesised by the reduction of mixed metal oxides under 10% hydrogen in argon at moderate temperatures (approx. 450 °C). The route affords some control over the stoichiometry of the product. High purity binary phases formed include $CoSb_3$, CoSb, NiSb, Cu_2Sb and SnSb. Owing to the significantly different reduction temperatures of the starting metal oxides, Mo_3Sb_7 was formed with impurities of MoO_2 and Sb metal. $CoSb_2$ and $NiSb_2$ were formed with impurities of $CoSb_3$ and NiSb, respectively.

1. Introduction

Transition metal antimonides have been shown to exhibit properties that can be utilised in a range of applications. Some of these properties include thermoelectric behaviour [1], semiconductivity [2] and superconductivity [3]. There is also evidence which demonstrates the potential for transition metal antimonides to be used as lithium ion battery anode materials [4–6]. Transition metal antimonides are therefore of great interest to industry and to the academic community.

Current synthetic routes to transition metal antimonides vary, but often involve the use of high temperatures, multi-step reactions and/or reaction under vacuum. The traditional route to transition metal antimonides is the direct reaction of the elements under vacuum. A survey of current literature reveals that reaction temperatures of around 1000 °C are common [3,7], although temperatures a little lower than this are sometimes employed [8]. Other alternatives which have been explored include metathesis [9], spark plasma sintering (SPS) [10,11], co-precipitation [12], solvothermal synthesis [13,14], mechanical alloying [15] and levitation melting [4]. The lattice enthalpy of the products is the driving force for the metathesis reaction of Na_3Sb with transition metal halides, which is initiated at temperatures up to 500 °C [9]. Spark plasma sintering uses a pulsed DC current as the heat source for the reaction. The formation of $CoSb_3$ in this way requires the use of an argon atmosphere or a vacuum to prevent oxidation of the elemental starting materials [10,11]. The same condition is required for the process of mechanical alloying, where elemental powders are dry milled and violently deformed by grinding [15]. Levitation melting, used to prepare CoSb, also requires the use of an argon atmosphere, and, in addition, requires the use of moderate temperatures (500 °C) for a prolonged period of time (7 days) [4]. Co-precipitation of cobalt oxalate and antimony sesquioxide provides another method of forming $CoSb_3$ [12]. However, co-precipitation is a multi-step process, and also requires the use of moderate temperatures (350–600 °C) to calcine and reduce the product. Solvothermal routes to transition metal antimonides also require several synthetic steps [13,14].

There is considerable interest in finding low temperature routes to these solids. We have developed a new synthetic route to transition metal antimonides which eliminates the need for high temperatures and reaction under vacuum, and potentially allows access to materials which melt incongruently. The method is an adaptation of previous work conducted on the reductive synthesis of transition metal nitrides, where intimately mixed metal oxides were reduced under an atmosphere of 10% hydrogen in nitrogen [16–19]. Here we report the facile synthesis of transition metal antimonides by the reduction of mixtures of metal oxides under 10% hydrogen in argon. We also demonstrate the ability to control product stoichiometry using this synthetic route. Frequently in solid-state compounds, small changes in composition can lead to large changes in physical properties. The synthesis and control of stoichiometry in new ternary intermetallics are therefore fundamental to optimisation of their properties.

Compounds that we have targeted using this synthetic procedure include binary and ternary antimonides of cobalt, nickel,

* Corresponding author. Tel.: +44 1482 466389; fax: +44 1482 466410.
E-mail address: T.Prior@hull.ac.uk (T.J. Prior).

0925-8388/$ – see front matter © 2010 Elsevier B.V. All rights reserved.
doi:10.1016/j.jallcom.2010.06.078

Table 1
Heating protocols for all compounds.

Compound	Firing 1	Firing 2	Firing 3	Firing 4
CoSb	425 °C (48 h)	450 °C (24 h)	–	–
$CoSb_2$	425 °C (48 h)	450 °C (24 h)	–	–
$CoSb_3$	425 °C (48 h)	450 °C (24 h)	450 °C (24 h)	–
NiSb	425 °C (48 h)	450 °C (24 h)	450 °C (24 h)	–
$NiSb_2$	425 °C (48 h)	450 °C (24 h)	475 °C (24 h)	475 °C (24 h)
Cu_2Sb	400 °C (48 h)	425 °C (24 h)	–	–
Mo_3Sb_7	425 °C (48 h)	450 °C (24 h)	475 °C (24 h)	520 °C (24 h)
SnSb	425 °C (48 h)	425 °C (24 h)	–	–
$Co_{1-x}Ni_xSb$	425 °C (48 h)	450 °C (24 h)	450 °C (24 h)	500 °C (24 h)

copper, molybdenum and tin; specifically $CoSb_3$, $CoSb_2$, CoSb, NiSb, $NiSb_2$, Cu_2Sb, Mo_3Sb_7, SnSb and the solid solution $Co_{1-x}Ni_xSb$. The binary compositions have previously been investigated for their potential use in technological applications. For example, $CoSb_3$ is well known for its thermoelectric behaviour; 'stuffing' the structure with weakly bonded atoms (such as Sn) increases the thermoelectric figure of merit by reducing the thermal conductivity of the material [20]. Similarly, Mo_3Sb_7 has attracted interest because it is a high temperature thermoelectric material that is an outstanding candidate for power generation [21,22]. In addition, CoSb, NiSb and Cu_2Sb have been investigated for their use as lithium ion battery anode materials [4–6].

2. Experimental

2.1. Synthesis

Reagents were purchased from Alfa Aesar in the following purities: cobalt oxide (Co_3O_4, 99.7%), nickel oxide (NiO, 99.998%), copper oxide (CuO, 99.995%), molybdenum trioxide (MoO_3, 99.9995%), tin oxide (SnO, 99%), antimony sesquioxide (Sb_2O_3, 99.999%).

Stoichiometric amounts of the appropriate metal oxides were accurately weighed, intimately ground until visibly homogeneous, and pelletised under a pressure of 440–740 GPa. In each case the amounts of starting reagents were calculated in order to form 1 g of product. After pelletising, the samples were heated (at a ramp rate of 3 °C/min) using the heating protocols given in Table 1 under a flow ($1.7(1)\,m^3\,h^{-1}$) of 10% hydrogen in argon (Energas) at each stage. Furnaces were allowed to cool radiatively to room temperature. Samples were handled in air with no special precautions taken, and re-ground and re-pelletised in between firings in order to maximise homogeneity.

2.2. Characterisation

Samples were analysed by X-ray powder diffraction using a Siemens D5000 diffractometer operating with Cu Kα radiation. Finely ground samples were mounted with a minimum of grease (Dow Corning® High Vacuum Grease) on a glass sample mount and rotated at 15 revolutions per minute during data collection. Diffraction patterns obtained for $CoSb_3$, CoSb, NiSb and Cu_2Sb were recorded over the range $5 \leq 2\theta/^\circ \leq 120$, with a step size of 0.020°, and a counting time of 9.3 s. Diffraction patterns recorded for $CoSb_2$, $NiSb_2$, Mo_3Sb_7, SnSb and for the ternary compositions were collected for a shorter time (step size 0.020°, counting time 1.0 s) and were recorded over the narrower range of $5 \leq 2\theta/^\circ \leq 70$.

Rietveld refinement of the crystal structures was carried out using the GSAS suite of programs [23]. Backgrounds were fitted using a shifted Chebyshev polynomial, and peak shapes were modelled using a pseudo-Voigt function. Lattice parameters, a zero point correction, profile parameters and atomic positions were refined. In the majority of cases isotropic displacement parameters were also refined. In cases where this led to an unstable refinement the parameters were fixed at small positive values ($U = 0.025$). For Mo_3Sb_7 displacement parameters were set to zero. The peak cut-off points were set to 0.15% of the peak maximum. The quality of the fit to each observed diffraction pattern may be judged by the residual $R(F^2)$, defined as $\Sigma|F^2_{obs} - F^2_{calc}|/\Sigma|F^2_{obs}|$.

3. Results and discussion

High purity samples of $CoSb_3$, CoSb, NiSb and Cu_2Sb were prepared by the reduction of stoichiometric mixtures of metal oxides under 10% hydrogen in argon. Samples of $CoSb_2$, $NiSb_2$ and Mo_3Sb_7 were also prepared, but with some impurities. Ternary antimonides in the series $Co_{1-x}Ni_xSb$ ($0.1 \leq x \leq 0.9$) were also synthesised as pure phases. We believe that full crystallographic details for materials with these ternary compositions have not been reported previously. Crystal structure and Rietveld refinement data for all compounds are given in the Supplementary data.

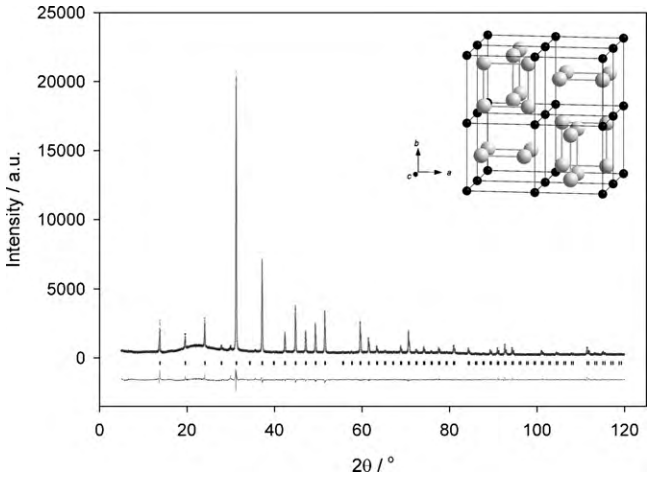

Fig. 1. Observed (crosses), calculated (grey line) and difference (black line) X-ray powder diffraction profiles for $CoSb_3$. Inset shows a representation of the skutterudite structure with Co in black and Sb in grey.

3.1. $CoSb_3$

$CoSb_3$ adopts the $CoAs_3$ (skutterudite) structure, crystallising in the cubic space group $Im\bar{3}$. The unit cell can be considered to be split into octants, with cobalt atoms positioned at the octant corners. Planar Sb_4 units, which are not quite square, occupy six out of eight of the octants, with the other two octants in the unit cell remaining empty. Filling of the empty octants with weakly bonded atoms (such as Sn) can cause a decrease in the thermal conductivity of the material, enhancing its thermoelectric behaviour.

$CoSb_3$ was made in good purity; a very small impurity peak was present in the diffraction pattern at approximately 30° two theta, that could be attributed to the phase Sb_6O_{13}. The presence of this phase is possibly a result of insufficient reduction. The Rietveld fit to the observed data is shown in Fig. 1. Good quality fit to the observed diffraction pattern was obtained as shown by an $R(F^2)$ value equal to 0.0792. A broad feature can be seen in the pattern centred on approximately 20–25° two theta. This was directly attributable to the sample mounting and not due to a poorly crystalline impurity in the sample. A diffraction pattern for the sample mount and comparison with Fig. 1 is given in the Supplementary information.

3.2. $CoSb_2$

$CoSb_2$ is the binary prototype for the arsenopyrite structure, a superstructure of the marcasite structure type [24], which was first established for FeAsS [25]. $CoSb_2$ crystallises in the monoclinic space group $P2_1/c$. The structure consists of distorted edge- and corner-sharing $CoSb_6$ octahedra. The distortion of the octahedra arises from a shifting of the Co atoms from the centres of the octahedra, resulting in alternately shorter and longer Co–Co distances, aligned almost parallel to the [1 0 1] direction [26].

The synthetic procedure yielded a product which was predominantly $CoSb_2$, but contained a small-scale impurity of $CoSb_3$; the product contained 82.2(9)% $CoSb_2$ by weight with 17.8(9)% $CoSb_3$. This reflects the great stability of $CoSb_3$ which forms under the reaction conditions. It may be that a slight alteration of the heating protocol may yield pure $CoSb_2$ preferentially. Good quality fit to the observed diffraction pattern was obtained as shown by an

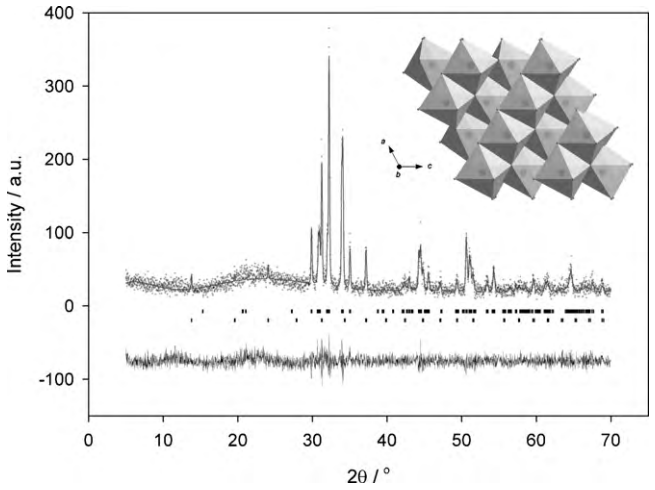

Fig. 2. Observed (crosses), calculated (grey line) and difference (black line) X-ray powder diffraction profiles for $CoSb_2$. The upper tick marks show the positions of allowed reflections from the main phase; lower ticks are those for $CoSb_3$. Inset shows a representation of the $CoSb_2$ structure (arsenopyrite) in terms of $CoSb_6$ octahedra.

$R(F^2)$ value equal to 0.1547. The multi-component Rietveld plot is shown in Fig. 2. The broad feature centred on 25° two theta is due to the sample mounting. (See Supplementary information).

3.3. NiSb and CoSb

NiSb and CoSb both adopt the nickel arsenide structure, crystallising in the hexagonal space group $P6_3/mmc$. The structure can be described as an *hcp* array of antimony in which the metal fills all of the octahedral holes.

The synthetic procedure yielded high purity NiSb and CoSb. The Rietveld fit for NiSb is shown in Fig. 3. Good quality fit to observed data was obtained as shown by an $R(F^2)$ value equal to 0.1062. We note the existence of a small unidentified broad feature at about 18° two theta in the diffraction pattern. This possibly indicates the presence of a poorly crystalline impurity. Good quality fit to the observed diffraction pattern for CoSb was also obtained as shown by an $R(F^2)$ value equal to 0.1367. Very small amounts of elemental cobalt and antimony (~0.5% by weight) were present. The Rietveld fit to CoSb is contained within the Supplementary data.

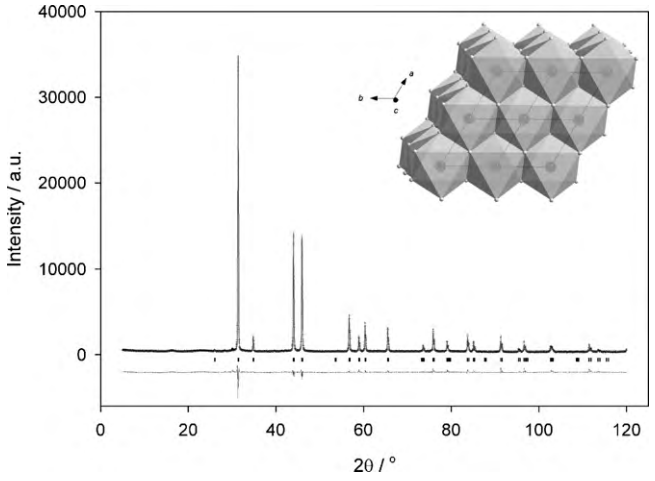

Fig. 3. Observed (crosses), calculated (grey line) and difference (black line) X-ray powder diffraction profiles for NiSb. Inset shows a representation of the nickel arsenide structure in terms of $NiAs_6$ ($NiSb_6$) octahedra.

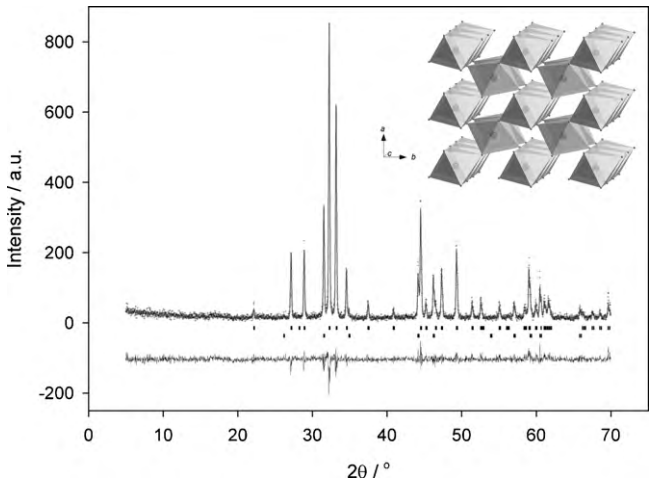

Fig. 4. Observed (crosses), calculated (grey line) and difference (black line) X-ray powder diffraction profiles for $NiSb_2$. The upper tick marks show the positions of allowed reflections from the main phase; lower ticks are those for NiSb. Inset shows a representation of the $NiSb_2$ structure (marcasite) in terms of $NiSb_6$ octahedra.

3.4. $NiSb_2$

$NiSb_2$ adopts the marcasite structure, crystallising in the orthorhombic space group *Pnnm*. The structure consists of corner-sharing chains of edge-sharing $NiSb_6$ octahedra, which run parallel to the *c* axis.

The synthetic procedure yielded a product which was predominantly $NiSb_2$, but contained a small-scale impurity of NiSb. The multi-component Rietveld plot is shown in Fig. 4. A good quality fit to the observed diffraction pattern was obtained as shown by an $R(F^2)$ value equal to 0.1181. It is interesting to note that NiSb, rather than $NiSb_2$, was formed in the initial stages of the reaction (450 °C). Due to the stoichiometric ratio of the starting reagents, unreacted antimony sesquioxide was also present after reaction at 450 °C. The formation of $NiSb_2$ began during reaction at 475 °C, and was accompanied by significant amounts of NiSb (40.5(5)% by weight) and antimony sesquioxide (24.4(5)% by weight). The final reaction at 475 °C resulted in a mixture of $NiSb_2$ (83.2(3)% by weight) and NiSb (16.7(3)% by weight). The presence of NiSb at this stage indicated that a small amount of antimony had been lost from the reaction. It is likely that the relatively high temperatures used to form $NiSb_2$ vapourised a small amount of antimony in the furnace. Further experimentation to optimise the preparation of $NiSb_2$ is underway.

3.5. Cu_2Sb

Cu_2Sb adopts the *anti*-PbFCl structure, crystallising in the tetragonal space group $P4/nmm$. The structure can be described in terms of edge-sharing $SbCu_9$ monocapped tetragonal antiprisms [7]. It can also be described in terms of layers of atoms on two distinct sites: the 2*a* and 2*c* Wyckoff positions. There are two copper sites (2*a* and 2*c*) and one antimony site (2*c*) in the Cu_2Sb structure. The copper and antimony atoms located on the 2*c* sites are arranged in a "corrugated" double layer, where the atom types alternate in all directions. This double layer is sandwiched by two square planar layers of copper atoms located on the 2*a* site. The copper atoms in the double layer are displaced very slightly towards the atoms in the all-copper plane, leading to the buckling of the layer [27].

Cu_2Sb was formed in high purity. However, upon close inspection, small impurity peaks can be observed in the diffraction pattern. These are too small to enable identification of the impurity phases. The Rietveld fit is shown in Fig. 5. Good quality fit to

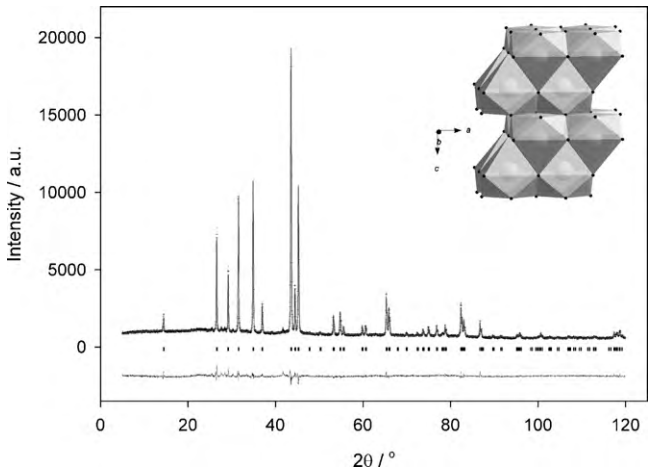

Fig. 5. Observed (crosses), calculated (grey line) and difference (black line) X-ray powder diffraction profiles for Cu_2Sb. Inset shows a representation of the Cu_2Sb structure in terms of $SbCu_9$ monocapped tetragonal antiprisms.

the observed diffraction pattern was obtained as shown by an $R(F^2)$ value equal to 0.1085.

3.6. Mo_3Sb_7

Mo_3Sb_7 adopts the Ir_3Ge_7 structure [3], crystallising in the cubic space group $Im\bar{3}m$. Häussermann et al. provide a detailed description of the structure of Mo_3Sb_7, which we have summarised below [28]. The Ir_3Ge_7-type structure is composed of atoms situated on three independent atomic positions, which are labelled T (12*e*), E1 (12*d*) and E2 (16*f*), with Mo atoms occupying the T site, and Sb atoms occupying the E sites. Two interpenetrating frameworks form the basis of the structure: the first is composed of T-centred square antiprisms, with E1 and E2 atoms at the vertices. Two of these square antiprisms share a square face forming a structure visually comparable to a 'barrel', with the rotation angle between the two square antiprisms equal to 45°. This angle is the same for all compounds adopting this structure. The 'barrels' are connected in such a way that an empty cube is formed as a junction between pairs of square antiprisms. The centres of these cubes are taken as the corners of the unit cell. The second framework is equivalent to the first, and is generated by the body-centring translation.

The synthetic procedure yielded a product which was predominantly Mo_3Sb_7, but contained impurities of MoO_2 (21(1)% by weight) and Sb (3(1)% by weight). The Rietveld fit to the observed data is shown in Fig. 6. Good quality fit to the observed diffraction pattern was obtained as shown by an $R(F^2)$ value equal to 0.1140. Attempts to refine displacement parameters within the main phase led to small negative U_{iso} values. Setting these values to 0.025 led to a clear and systematic mismatch with the observed data. The fit was considerably better (both judged by eye and in terms of the quality of fit parameters) when the U_{iso} values were set to zero and this model was retained in the final refinement. The presence of impurities of MoO_2 and Sb is likely to be a result of the significantly different temperatures at which molybdenum(VI) oxide and antimony sesquioxide reduce: antimony sesquioxide reduces at approximately 400 °C; molybdenum(VI) oxide reduces to molybdenum(IV) oxide quite easily at this temperature. However, the reduction of molybdenum(IV) oxide only occurs at above approximately 600 °C. Performing this reaction at a higher temperature than 600 °C leads to the reduction of antimony sesquioxide occurring too quickly, therefore forming elemental antimony. At present we have not been able to produce Mo_3Sb_7 without the presence of impurities due to the significant difference in ease of reduction of the metal oxides.

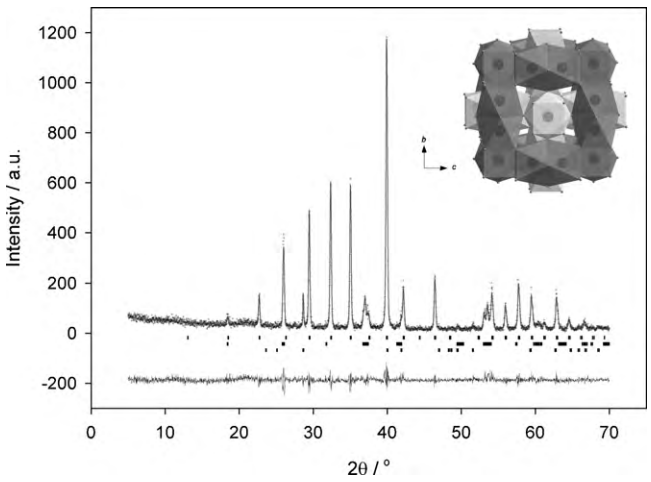

Fig. 6. Observed (crosses), calculated (grey line) and difference (black line) X-ray powder diffraction profiles for Mo_3Sb_7. The upper tick marks show the positions of allowed reflections from the main phase; middle ticks are those for MoO_2; lower ticks are those for Sb. Inset shows a representation of the Ir_3Ge_7-type structure.

3.7. SnSb

The structure of SnSb has recently been definitively studied [29]. The structure is incommensurate as a result of ordering of Sb and Sn within the structure. The parent structure is very close to that of α-Po. The 3-D space group is $R\bar{3}m$ although the structure is very close to cubic ($\alpha = \beta = \gamma = 89.7°$). The refinement used the 3-D space group formalism on account of the unavailability of synchrotron radiation to detect satellite reflections.

SnSb was formed in high purity. The isotropic displacement parameters of the antimony atom and the tin atom were constrained in the refinement to be equal due to both atoms occupying the same crystallographic site. The Rietveld fit is shown in Fig. 7. Good quality fit to the observed diffraction pattern was obtained as shown by an $R(F^2)$ value equal to 0.0959.

3.8. Ternary phases in the Co–Ni–Sb system

CoSb and NiSb both adopt the nickel arsenide structure. Owing to this and the similar size of cobalt and nickel, it was proposed that solid solutions in this system could be expected to form. Compositions of $Co_{1-x}Ni_xSb$ ($0.1 \leq x \leq 0.9$), with x increasing in increments of 0.1, were therefore synthesised. The Rietveld fit of one of the

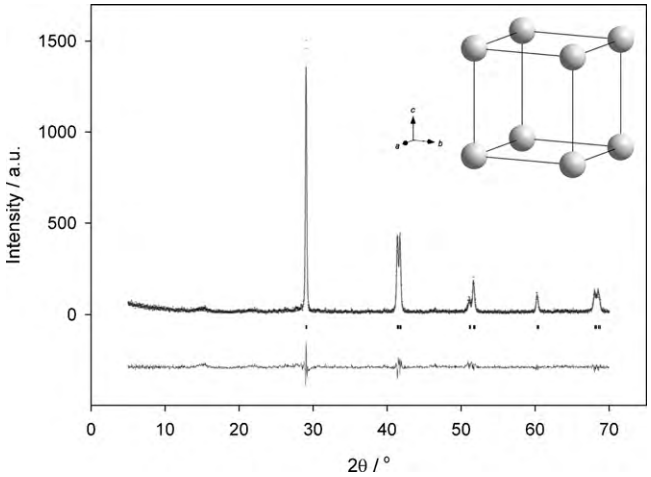

Fig. 7. Observed (crosses), calculated (grey line) and difference (black line) X-ray powder diffraction profiles for SnSb. Inset shows a representation of the SnSb structure.

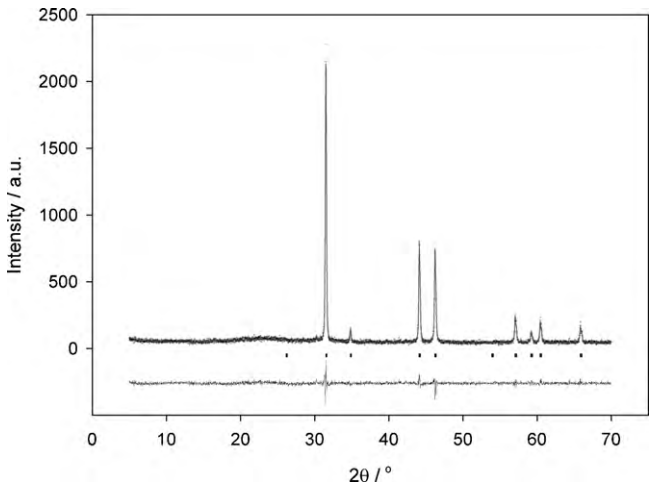

Fig. 8. Observed (crosses), calculated (grey line) and difference (black line) X-ray powder diffraction profiles for $Co_{0.5}Ni_{0.5}Sb$.

compositions in the series ($Co_{0.5}Ni_{0.5}Sb$) is shown in Fig. 8. Good quality fit to the observed diffraction pattern was obtained as shown by an $R(F^2)$ value equal to 0.0577.

Full width at half maximum values for each phase ($0 \leq x \leq 1$) were calculated for the (1 0 2) reflection located at approximately 44° two theta. Examination shows there is no significant variation in full width at half maximum across the series, strongly suggesting the presence of single phase products. $R(F^2)$ values for the series were all in the range 0.0515 to 0.1221. To our knowledge this is the first report of a crystallographic study of the solid solution of NiSb in CoSb.

The X-ray diffraction data indicate full miscibility of NiSb in CoSb. This is illustrated in the linear increase in unit cell volume with increasing nickel content shown in Fig. 9. Fig. 10 shows how the M–Sb and Sb–Sb bond lengths vary with composition.

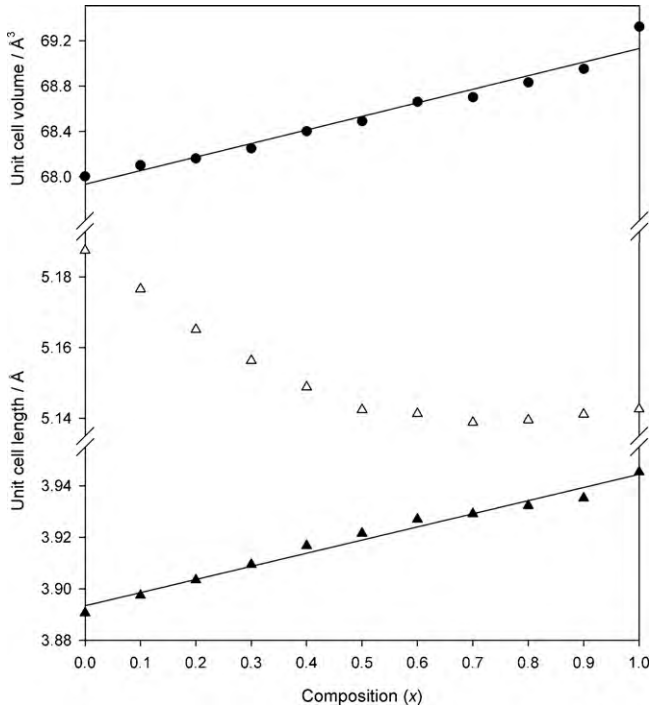

Fig. 9. Plot showing how the unit cell parameters *a* and *c*, and the unit cell volume, *V*, of $Co_{1-x}Ni_xSb$ vary with composition (*x*). Filled triangles represent *a*, unfilled triangles represent *c*, and circles represent the unit cell volume, *V*. Estimated standard errors on the parameters are too small to be visible.

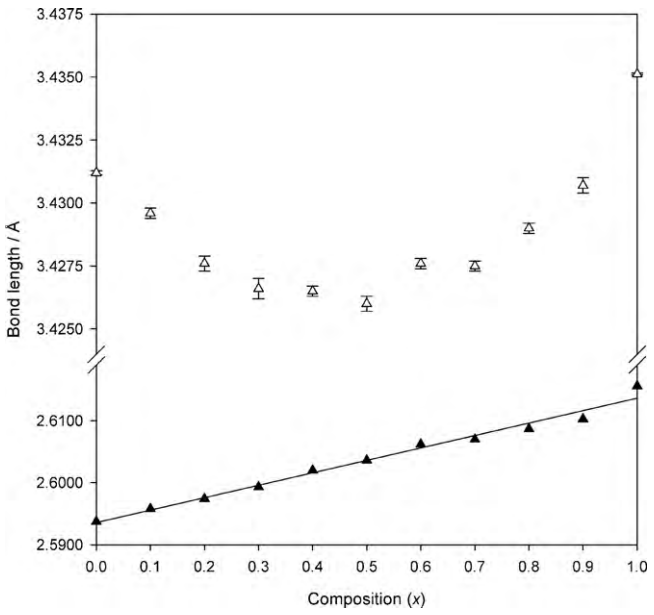

Fig. 10. Plot of M–Sb and Sb–Sb bond lengths against composition (*x*) for $Co_{1-x}Ni_xSb$. Filled triangles represent M–Sb bond lengths, and unfilled triangles represent Sb–Sb bond lengths.

The plots of unit cell length *a*, unit cell volume and M–Sb bond length against composition clearly show an almost linear relationship between the two variables. The steady increase in volume with increasing Ni content is mirrored in the M–Sb bond lengths which vary smoothly across the series. The variation in Sb–Sb distances is more surprising and does not follow the same linear trend. The Sb–Sb bond length reaches a minimum (3.4260(3) Å) at the composition $NiCoSb_2$, which signifies the strongest Sb–Sb bonding interaction in this phase. This is considerably longer than the Sb–Sb distance in elemental antimony recorded at 298 K (2.9082(5) Å) [30]. The variation of unit cell length *c* with composition does not follow a linear trend, but follows a decreasing trend until approximately $x = 0.5$, above which the value of *c* changes very little. At a similar value, the plot of the Sb–Sb bond length against composition reaches a minimum.

3.9. Discussion

The method described here provides a relatively low temperature route to binary and ternary antimonides by reduction of mixtures of binary oxides. It is similar to work carried out by Gopalakrishnan et al. [31] that describes the reduction of crystalline precursors with well-defined stoichiometry such as $NiSb_2O_6$ to give metal pnictides; a method applicable to a variety of binary compounds where suitable precursors can be found.

The synthetic method described here is akin to that of Gopalakrishnan, but does not require that precursors are made prior to reduction. Secondly, where binary oxides are the starting materials the synthesis of ternary or higher compounds is easily accomplished as in the case of $Co_{1-x}Ni_xSb$. Certainly in the case of the metal phosphides the purity of products reported by Gopalakrishnan is good. It may be that by careful alteration of the heating regime, the purity of products from our protocol can be further improved.

4. Conclusion

A new low temperature synthetic route to binary and ternary metal antimonides has been demonstrated. The binary phases $CoSb_3$, CoSb, NiSb, Cu_2Sb and SnSb were synthesised to a high

degree of purity. The phases $CoSb_2$, $NiSb_2$ and Mo_3Sb_7 were also synthesised albeit with impurities. Work to optimise the synthetic conditions and eliminate impurities is underway. The new series of pure ternary transition metal antimonides, $Co_{1-x}Ni_xSb$ ($0.1 \leq x \leq 0.9$), was also synthesized, and our results suggest there is a full miscibility range of NiSb in CoSb. To demonstrate the further utility of this method we are in the process of investigating the synthesis of ternary compositions reported to display a miscibility gap. Similarly, we are examining other antimonides reported to melt incongruently, such as NbIrSb and $AuSb_2$.

Acknowledgement

RLK is grateful to EPSRC for the provision of a Departmental Training Award to carry out this work.

Appendix A. Supplementary data

Supplementary data associated with this article can be found, in the online version, at doi:10.1016/j.jallcom.2010.06.078.

References

[1] Y. Kawaharada, K. Kurosaki, M. Uno, S. Yamanaka, J. Alloys Compd. 315 (2001) 193–197.
[2] T. Caillat, A. Borshchevsky, J.P. Fleurial, J. Appl. Phys. 80 (1996) 4442–4449.
[3] Z. Bukowski, D. Badurski, J. Stępień-Damm, R. Troć, Solid State Commun. 123 (2002) 283–286.
[4] J. Xie, G.S. Cao, X.B. Zhao, M.J. Zhao, Y.D. Zhong, L.Z. Deng, Y.H. Guan, Z.T. Wu, J. Mater. Sci. 39 (2004) 1105–1107.
[5] J. Xie, X.B. Zhao, H.M. Yu, H. Qi, G.S. Cao, J.P. Tu, J. Alloys Compd. 441 (2007) 231–235.
[6] L.M.L. Fransson, J.T. Vaughey, R. Benedek, K. Edstrom, J.O. Thomas, M.M. Thackeray, Electrochem. Commun. 3 (2001) 317–323.
[7] J. Nuss, U. Wedig, M. Jansen, Z. Kristallogr. 221 (2006) 554–562.
[8] C. Candolfi, B. Lenoir, A. Dauscher, J. Tobola, S.J. Clarke, R.I. Smith, Chem. Mater. 20 (2008) 6556–6561.
[9] A.L. Hector, I.P. Parkin, Z. Naturforsch. B: Chem. Sci. 49 (1994) 477–482.
[10] C. Recknagel, N. Reinfried, P. Höhn, W. Schnelle, H. Rosner, A. Yu Grin, Leithe-Jasper, Sci. Technol. Adv. Mater. 8 (2007) 357–363.
[11] J.X. Zhang, Q.M. Lu, K.G. Liu, L. Zhang, M.L. Zhou, Mater. Lett. 58 (2004) 1981–1984.
[12] M. Wang, M. Yu Zhang, Muhammed, Nanostruct. Mater. 12 (1999) 237–240.
[13] J.L. Mi, X.B. Zhao, T.J. Zhu, J.P. Tu, G.S. Cao, J. Alloys Compd. 417 (2006) 269–272.
[14] C. Li, J. Hu, Q. Peng, X. Wang, Mater. Chem. Phys. 110 (2008) 106–109.
[15] P. Amornpitoksuk, S. Suwanboon, J. Alloys Compd. (2009) 373–375.
[16] T.J. Prior, P.D. Battle, J. Solid State Chem. 172 (2003) 138–147.
[17] T.J. Prior, S.E. Oldham, V.J. Couper, P.D. Battle, Chem. Mater. 17 (2005) 1867–1873.
[18] S.E. Oldham, P.D. Battle, S.J. Blundell, M.L. Brooks, F.L. Pratt, T.J. Prior, J. Mater. Chem. 15 (2005) 3402–3408.
[19] T.J. Prior, P.D. Battle, J. Mater. Chem. 14 (2004) 3001–3007.
[20] R.C. Mallik, J.-Y. Jung, S.-C. Ur, I.-H. Kim, Met. Mater. Int. 14 (2008) 615–620.
[21] C. Candolfi, B. Lenoir, A. Dauscher, Phys. Rev. B 79 (2009) 035114.
[22] H. Xu, K.M. Kleinke, T. Holgate, H. Zhang, Z. Su, T.M. Tritt, H. Kleinke, J. Appl. Phys. 105 (2009) 053703.
[23] A. C. Larson, R. B. Von Dreele, General Structure Analysis System (GSAS), Los Alamos National Research Laboratory Report LAUR 86-748, 1994.
[24] E. Makovicky, in: D.J. Vaughan (Ed.), Sulfide Mineralogy and Geochemistry, Mineralogical Society of America, Chantilly, Virginia, 2006, pp. 7–125, ISBN is 0-939950-73-1 (Reviews in Mineralogy and Geochemistry 61).
[25] M.J. Buerger, Z. Kristallogr. 95 (1936) 83–113.
[26] A. Kjekshus, Acta Chem. Scand. 25 (1971) 411–422.
[27] W.N. Stassen, M. Sato, L.D. Calvert, Acta Crystallogr. Sect. B: Struct. Sci. 26 (1970) 1534–1540.
[28] U. Häussermann, M. Elding-Pontén, C. Svensson, S. Lidin, Chem. Eur. J. 4 (1998) 1007–1015.
[29] L. Norén, R.L. Withers, S. Schmid, F.J. Brink, V. Ting, J. Solid State Chem. 179 (2006) 404–412.
[30] C.S. Barrett, P. Cucka, K. Haefner, Acta Cryst. 16 (1963) 451–453.
[31] J. Gopalakrishnan, S. Pandey, K. Kasthuri, Chem. Mater. 9 (1997) 2113–2116.